Journal of Engineering Science and Technology
Vol. 18, No. 1 (2023) 481 - 507

CHARACTERIZATION OF LEAD OXIDE MILLED NANOPARTICLES AND THE EFFECT OF THEIR INCORPORATION ON THE THERMAL PROPERTIES OF POLYSTYRENE

AHMAD FIRAS OSMAN[1, 2,*], ALAA M. ABDALLAH[1], MOHAMED. S. BADAWI[1], MOHAMAD ROUMIE[2] RAMADAN AWAD[1,3]

[1]Department of Physics, Faculty of Science, Beirut Arab University, 1107 2809 Beirut, Lebanon
[2]Lebanese Atomic Energy Commission, National Council for Scientific Research, Riad El Solh 1107 2260 Beirut, Lebanon
[3]Physics Department, Faculty of Science, Alexandria University, 21511 Alexandria, Egypt
*Corresponding Author: a.f.osman@cnrs.edu.lb

Abstract

In this study, different nano sizes of lead oxide particles are prepared using high-speed planetary ball milling over a range of grinding times (15, 30, 60 and 120 minutes). The characterization of the prepared nanoparticles is carried out using X-ray diffraction (XRD), transmission electron microscopy (TEM), dynamic light scattering (DLS) and Fourier Transform-Infrared spectroscopy (FTIR). The XRD pattern reveals a phase transition from β-PbO to α-PbO with increasing the milling time. The PbO particles milled for 30 and 60 minutes and termed PbO(A) and PbO(B), respectively, are chosen for this research as they display less agglomeration and achieve nano sizes of 78 and 52 nm, respectively. The following stage utilizes PbO(Bulk), PbO(A) and PbO(B) as fillers and incorporates them independently into PS with a concentration of 10, 15, 25 and 35 wt % using roll mill mixing and compression moulding techniques to create a novel polystyrene composite (PS/PbO). PS/PbO composites were then characterized by XRD, which shows a decrease in the phase percentage of PS to α-PbO with increasing PbO content. Extensive research of thermal characteristics employing thermogravimetric analysis (TGA) and differential scanning calorimetry (DSC) enables the evaluation of decomposition rates and activation energies. The analysis reveals that the addition of bulk and nano PbO particles shifts T_{ini} and $T_{50\%}$ to higher temperatures and reduces the decomposition rate as well as the activation energy. This means that the thermal stability of PS is increased, especially using a small PbO nano size. This work focuses on the manufacture and characterization of various nano-sized PbO as well as the impact of their incorporation on the thermal properties of polystyrene, which will be examined as X-ray shields.

Keywords: Ball milling, PbO nanoparticles, Polystyrene based composite, TGA, XRD.

1. Introduction

For the last two decades, polymer nanocomposites have attracted the focus of many researchers due to their exceptional properties when compared to pure polymers or traditional composites. Nanoparticles exhibit distinctive properties attributable to their high surface area-to-volume ratio. Numerous aspects, such as the size and load of the incorporated nanoparticles, as well as the preparation methods, affect the characteristics and functionality of the nanocomposite [1-3]. Polymer nanocomposites are a novel class of materials that are widely used in a variety of fields of research and industry such as automobiles, aerospace, coatings, adhesives, fire-retardants, packaging, drug delivery, sensors, medical devices [4-5] and radiation shielding [6-8].

Polystyrene (PS), $(C_8H_8)_n$, belongs to the thermoplastic amorphous polymer family and is well recognized in the field of packaging and thermal insulation due to its resistance to thermal degradation. Besides, the importance of PS is based on its physical properties, particularly light-weight, flexible, low cost, processability and recycling. These reflect an eco-friendly behavior towards human health and the environment [9, 10]. Among the fillers incorporated with PS, lead was chosen since the new polymer nanocomposite will be evaluated for radiation attenuation capability [11]. Lead mono oxide (PbO) has received considerable research attention in all lead oxide forms as it is a semiconductor with two crystalline structures: litharge (tetragonal crystalline structure) with a bandgap of 1.9-2.2 eV and massicot (orthorhombic crystalline structure) with a bandgap of 2.7 eV [12]. Lead mono oxide has been used in many applications such as laser technology, electrocardiography, imaging devices, batteries, paints, glass industry and radiation shielding [13-15]. On the other hand, lead oxide nanoparticles are categorized as toxic and hazardous to humans and the environment, even though may act as effective anticancer and antimicrobial agents [16].

Many researchers have studied the thermal properties of PS-based composites; Kreutz et al. [17] examined the effect of fiber content on the thermal properties of polystyrene reinforced with medium-density fiberboard (MDF). They discovered that even though the presence of MDF improved the thermal stability of PS, the weight percentage of MDF did not affect the composite's degradation temperature.

Ahmad et al. [18] used the solution casting method to prepare thin sheets of waste Polystyrene (WPS) composite with different weight fractions of copper oxide nanoparticle (CuO) and reduced graphene oxide (rGO). They investigated the effect of the filler weight ratios on the thermal properties of the composite. TGA analysis revealed that at 250-400°C, the weight losses of WPS-rGO-CuO:2% and WPS-rGO-CuO:15% were 22.02 and 20.01%, respectively, whereas WPS showed a weight loss of 73.36%. This result is due to pyrolysis and polymer chain degradation, showing that the fabricated composite has excellent thermal stability compared to WPS.

Farha et al. [19] reported the use of Zinc oxide (ZnO) nanorods, prepared by sol-gel route, as fillers in the synthesis of polystyrene nanocomposites (PS/ZnO) using the casting method. The results of TGA and DSC confirmed that the addition of ZnO nanorods within a concentration range (0, 0.5, 0.7, 1 and 3 wt%) enhanced the thermal stability of PS and the most thermally stable nanocomposites were obtained at 1 wt% of ZnO nanorods by a delay of 10°C in thermal degradation.

Karimabad et al. [20] mentioned that silicon dioxide (SiO_2) nanoparticles, synthesized by sol-gel process and then added to the PS polymer matrix, exhibited good performance in flame retardancy. The investigation of TGA showed that the thermal decomposition of the PS-SiO_2 composite was shifted towards a higher temperature (370 °C) due to the presence of tin oxide.

Suresh et al. [21] prepared organo-functionalized Nickel Aluminide (Ni-Al) layered double hydroxide (LDH)-polystyrene (PS) nanocomposites using co-precipitation and melt intercalation techniques. The DSC and TGA analysis indicated that the addition of Ni-Al LDH into the PS enhanced the glass transition temperature T_g and the degradation temperature T_d gradually by increasing the filler content (1, 3, 5 and 7 wt%). For the nanocomposite with 7 wt% Ni-Al LDH loading, T_g was 4.3 °C higher than that of PS and T_d was enhanced by 27.4 °C concerning PS.

El Gamal et al. [22] used solution casting to prepare PbO/PVC/PMMA nanocomposite films. They reported the influence of PbO loading (0.5 to 4 wt%) on the thermal properties of the nanocomposite. TGA analysis revealed that the maximum improvement in thermal stability was for nanocomposite with 2 wt% of PbO load with T_{onset} = 280.5, $T_{10\%}$ = 300.8 and $T_{50\%}$ = 377.9 °C, whereas degradation temperatures of PS/PMMA blend were T_{onset} = 268.9, $T_{10\%}$ = 280.6 and $T_{50\%}$ = 361.9 °C.

Mahmoud et al. [23] investigated the effect of adding either micro or nano-sized lead oxide (PbO) on the thermal properties of high-density polyethylene (HDPE). They discovered that increasing the PbO filler increased the degradation temperatures (T_{ini} and $T_{50\%}$), which reached their maximum at 50 wt% loading of PbO-NPs and bulk PbO. PbO-NPs had the greatest influence on the thermal properties of the composites, as they showed an increment of 18.2% and 4.1% for T_{ini} and $T_{50\%}$, respectively, whereas incorporating PbO bulk increased the values of T_{ini} and $T_{50\%}$ by 15.7% and 3.6%, respectively.

The conventional chemical methods used to prepare PbO nanoparticles are expensive and produce low yield [24]. In the present study, a new PS/PbO composite is prepared using a simple and cost-effective technique by incorporating a large amount of PbO nanoparticles of various sizes, synthesized by high-speed planetary ball milling, into PS with different filler loads (0, 10, 15, 25, and 35 wt%) via compressing moulding. In addition to size, the structural characteristics, morphology, and chemical bonding of the synthesized PbO nanoparticles are determined. The novel PS/PbO will be examined for X-ray attenuation capability; hence the investigation of thermal and mechanical properties is essential. The influence of PbO particle size on the thermal properties of PS/PbO is investigated, highlighting thus the role of particle nano size and concentration in improving the thermal properties of the composite.

2. Materials and Methods

2.1. Materials

Commercial Polystyrene (PS) purchased from Egyptian Styrene and Polystyrene Production, with a density of 1.03 g/cm^3 and melt flow rate of 11.1 g/10 minutes, was used as a polymer matrix. Lead (II) oxide (PbO) from Sigma-Aldrich, Yellow powder with purity ≥ 99.0%, Molecular weight 223.20 g/mole and density = 9.53 g/cm^3, was used for the synthesis of PbO nanoparticles used as filler in the composite.

2.2. PbO nanoparticle synthesis

A high-speed planetary ball milling machine (Retsch, PM 100, Germany) was used for the preparation of PbO nanoparticles. The milling operation was performed in a 250 ml zirconium oxide jar. The weight ratio of the zirconium ball to powder was 10:1, and the angular velocity was set to 400 rpm. The milling process was carried out at 4 different milling times (15, 30, 60, and 120 minutes). Each milling phase consisted of a five-minute grind followed by a one-minute pause to prevent metal oxide particles from overheating and agglomeration.

2.3. PS/PbO composite preparation

PS/PbO composite was prepared using the compression moulding technique by adding various amounts (0, 10, 15, 25, and 35 wt%) of PbO(Bulk) or PbO nanoparticles with different sizes. In this method, PbO filler and Polystyrene with appropriate proportions were sensitively weighed and mixed thoroughly in a two-roll mill mixer (XK400, Shandong, China) at 200 °C for 30 minutes at 50 rpm speed for appropriate filler distribution. The sample was gathered, ground, and spilled into a mold of stainless steel (25×25×0.3 cm3) and placed between Teflon layers to get a smooth surface. The next step consists of hot pressing the sample for 15 minutes at 200 °C and 20 MPa by applying the hydraulic press. After sintering, the shaped composite sample was gradually cooled to ambient temperature under compression for 15 minutes.

2.4. Characterization and thermal properties analysis

Paragraph 2.4 summarizes the experimental methodologies used to characterize PbO particles and PS/PbO composites and investigate their thermal properties.

2.4.1. X-ray diffraction (XRD)

The structural properties and the size of PbO ground particles were determined by X-ray diffraction XRD (Model: D8 FOCUS BRUKER, USA) using Cu-kα as a source of radiation (λ = 0.154 nm). The study was performed between $10^{o} \leq 2\theta \leq 70^{o}$ with increment step = 0.02° and exposure time = 1s, and the X-ray tube was operated at 40 kV and 40 mA.

2.4.2. Transmission electron microscopy (TEM)

The morphological aspect and the size of the synthesized PbO particles were studied using a transmission electron microscope (JEOL, JEM-2100F, Japan), operated at 200 kV. The PbO powder was dissolved in ethanol using ultrasound and deposited directly onto a Cu grid.

2.4.3. Dynamic light scattering (DLS)

Dynamic light scattering DLS, otherwise known as quasielastic light scattering, was performed using Nano Plus (Particulate systems, Japan) to investigate the size distribution, stability, and aggregation state of PbO particles.

2.4.4. Fourier transform-infrared spectroscopy (FTIR)

FTIR (Bruker Vertex 70, USA) was employed to study the chemical bonds, characteristic peaks, and functional groups of the PbO particles and the prepared composite. The beam from an IR source pass through a monochromatic controller, ensuring that only specified wavelengths are emitted, with a varying range (4000 - 500 cm-1). The Nano-sized particles are placed in a holder in the path of the IR source. The data acquisition of the FTIR spectrometer is based on parallel running dual-channel delta-sigma ADC´s with a 24-bit dynamic range that is integrated into each detector. This advanced DigiTectTM technology intercepts external signal disturbance and guarantees a PEAK signal-to-noise ratio.

2.4.5. Thermogravimetric analysis (TGA)

Thermogravimetric analysis (TGA) using (NETZSCH, TG 209F1 Libra, Germany) was performed to investigate the thermal stability of the PS/PbO synthesized composites. A sample mass of 10-15 mg was collected and placed in alumina (Al2O3) crucibles, which were heated from 30 to 600 °C in a pure nitrogen atmosphere at a heating rate of 10 °C/minute. Temperatures corresponding to 5% (T_{ini}) and 50% ($T_{50\%}$) weight loss of the sample were investigated.

2.4.6. Differential scanning calorimetry (DSC)

The Differential scanning calorimetry (DSC) measurements of the PS/PbO composites were carried out using (Shimadzu DSC-60A, Japan). The examined samples typically weighed around 3-5 mg, were placed in an aluminum pan and heated at a continuous rate of 10 °C/minute throughout a temperature range of 30 to 200 °C under a nitrogen environment.

3. Results and Discussion

The subsequent section describes the main findings in the test results, interprets them, and discusses the importance of the findings. It will be divided into two parts: the characterization of lead oxide powder followed by the characterization of PS/PbO composites and their thermal properties.

3.1. PbO particles characterization

First, the outcomes of experimental characterization studies on lead oxide particles ground at different times are explained.

3.1.1. XRD analysis

The X-ray diffraction patterns of bulk PbO(Bulk) and PbO particles ground at various times is revealed in Fig. 1. These patterns are refined using the Material Analysis Using Diffraction (MAUD) software, to identify the presented phases in the samples. The refinements showed the presence of both PbO phases, the yellow massicot β-PbO phase and the red litharge α-PbO phase. It is noticed that the pattern of the bulk PbO sample mainly reflects the β-PbO phase, with Bragg peaks at 29.2˚, 30.4˚, 32.7˚, 37.9˚, 45.2˚, 49.4˚, 50.9˚, 53.2˚, 56.1˚, 60.4˚, and 63.2˚, corresponding to planes (101), (020), (200), (201), (220), (022), (202), (131), (311), (222), and (212). These crystallographic reflections are consistent with the ICDD (JCPDS)

Card No. 00-038-1477 of orthorhombic pure massicot phase lead oxide and previous literature [25, 26]. Otherwise, the XRD patterns of ground PbO particles revealed incomplete phase transformation from orthorhombic massicot β-PbO phase (ASTM 05-0570) to tetragonal litharge α-PbO phase (ASTM 05-0561) [27, 28]. The additional Bragg peaks at 2θ = 28.72˚, 32˚, 35.8˚, 48.7˚, 54.9˚ and 59.46˚ in the XRD pattern of the ground PbO particles were the reflection of tetragonal litharge phase, corresponding to planes (111), (200), (002), (202), (311), and (222), which are consistent with the JCPDS Card No. 00-005-0561 [29]. These changes in the phase percentages are listed in Table 1. The phase percentage of β-PbO decreased monotonously from 97.78 to 1.42%, accompanied by an increase in the phase percentage of α-PbO from 2.21 to 98.57%, as the milling time increased from zero to 120 minutes. Hence, there is a partial phase transition by the effect of milling due to the exerted pressure on the powders [30]. This pressure generated crystal defects, including dislocations, stacking faults, stresses and pores. Additionally, more lattice defects and micro-strains are created, mainly due to the plastic deformation by the effect of milling [31].

The refined lattice parameters of both β-PbO and α-PbO phases, listed in Table 1, confirm the orthorhombic and the tetragonal structure with space groups of Pb cm and p4/nmm, respectively [32]. The obtained lattice parameters for the orthorhombic phase (a, b and c) and the tetragonal phase (a and c), match with previous literature [33, 34]. Moreover, the b/a and c/a ratios were calculated for the orthorhombic β-PbO phase and it is found to be almost constant (b/a = 0.93 and c/a = 0.806) with the increase in milling time, meaning that there are slight changes in the orthorhombic structure. Similarly, the c/a ratio of the tetragonal α-PbO phase fluctuated around 1.26, indicating negligible changes in the lattice parameters by the effect of milling. Moreover, the highlight of Fig. 1 shows the reduction of the intensity and broadening of the peaks as the mechanical milling time increased. These changes in the peak profile are linked to changes in the size and micro-strain values. Hence, the crystallite size is calculated using *DIFFRAC.EVA* and *TOPAS* software and the micro-strain values are extracted from the refinements (MAUD software), to understand these changes.

The estimated values are listed in Table 2. The crystallite size decreased with increasing grinding time, reaching 54 nm after 60 minutes, followed by a slight increase at 120 minutes. This is accompanied by the increase of the micro-strain values for both β-PbO and α-PbO phases with increasing milling time to 60 minutes, followed by an insignificant reduction at 120 minutes. Therefore, the milling reduced the sizes and initiated micro-strains in the powders, following the trend obtained by previous studies [35-38].

These variations are mainly attributed to the generated plastic deformation by the effect of milling and hence, increasing the disorder and crystal defects of the powdered particles [35, 36]. These crystal defects include dislocations and stacking faults, that arise with increasing the milling time, leading to misorientations between sub-grains and hence, forming particles with smaller sizes and larger micro-strains [35]. However, after 120 minutes of milling, the crystallite size increased and the micro-strain value decreased, mainly due to the agglomeration of the particles, in an attempt to lower their surface energy state. Mathew et al. [39] discovered that the sizes of PbO particles prepared by chemical and biological synthesis were 180 nm and 78 nm, respectively. Akimov et al. [40] produced PbO nanoparticles using the thermal decomposition method and obtained a PbO nanoparticle size range of 60 to 100 nm.

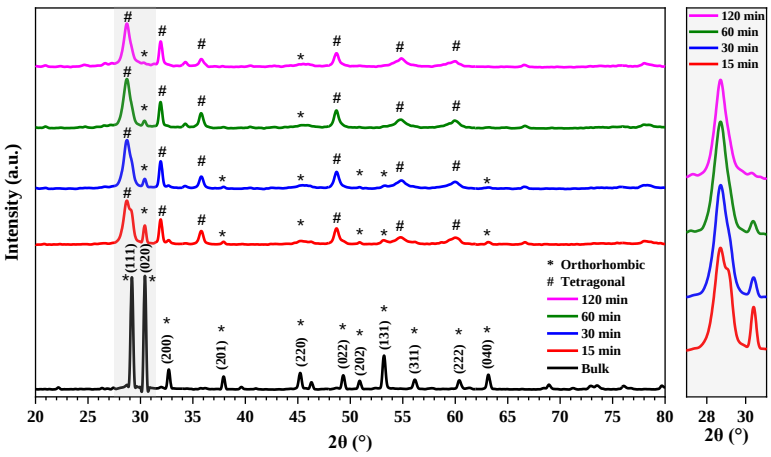

Fig. 1. The X-ray diffraction pattern of bulk PbO and PbO particles ground for 15, 30, 60 and 120 minutes.

Table 1. The extracted and computed structural parameters from the XRD analysis of PbO particles.

Grinding time (minutes)		Bulk	15	30	60	120
β-PbO	Phase %	97.78	23.96	17.39	6.33	1.42
	a (Å)	5.886	5.897	5.878	-	-
	b (Å)	5.484	5.497	5.498	-	-
	c (Å)	4.749	4.755	4.749	-	-
	c/a	0.806	0.806	0.808	-	-
	b/a	0.932	0.932	0.935	-	-
	$\eta\times 10^{-3}$	0.335	0.981	1.002	-	-
α-PbO	Phase %	2.22	76.04	82.61	93.67	98.58
	a (Å)	-	3.976	3.969	3.976	3.980
	c (Å)	-	5.028	5.0204	5.024	5.030
	c/a	-	1.264	1.265	1.263	1.264
	$\eta\times 10^{-3}$	-	3.819	3.960454	4.058	2.170

3.1.2. TEM analysis

The TEM micrographs of bulk PbO and PbO particles milled at different times (15, 30, 60 and 120 minutes) are illustrated in Figs. 2(a)-(e). The micrographs demonstrated that PbO (Bulk) is shaped differently than the ground PbO particles, which is verified by the XRD results that showed an orthorhombic structure for PbO (Bulk) and a tetragonal structure for the ground PbO. Furthermore, the micrographs revealed that the size of the PbO granules decreased as the grinding time increased, with a tendency to agglomerate at high grinding times (120 minutes). The size of particles in the TEM micrographs was measured using ImageJ software, and the average particle size (D_p) was calculated from the Gaussian distribution function of the size histograms. As shown in Table 2, the dimensions of the PbO particles milled for 15, 30, 60 and 120 minutes were respectively 100.87, 78.17, 52.56 and 58.36 nm. A comparison of particle sizes calculated by XRD, and TEM revealed a high degree of consistency between the two measurement techniques.

3.1.3. DLS analysis

Dynamic Light Scattering (DLS) analysis was used to further investigate the size changes, distributions, and aggregations that occurred during the mechanical milling process. Figures 3(a)-(e) depict the DLS spectra of bulk PbO and PbO powder milled at various milling times. Two discernible particle sizes were revealed in each DLS spectrum of PbO particles milled at 15 and 120 minutes as shown in Figs. 3(b) and (e). Particle sizes are comparable and have remarkable intensity distributions, indicating moderate aggregation. However, Figs. 3(c) and (d) showed that the particle sizes in DLS spectra of PbO particles milled at 30 and 60 minutes are not close, and the high-intensity distribution is attributed to the smallest size, and, hence exhibiting low aggregation.

Crystallinity which can be evaluated from XRD and TEM techniques is defined as the degree of structural order in a solid. By comparing the crystallite size resulting from XRD data as well as from TEM, the crystallinity Index (I_{cry}) is calculated using Eq. (1)

$$I_{cry} = \frac{D_p}{D} \tag{1}$$

where D_p is the particle size obtained from TEM micrographs and D is the particle size obtained from the XRD technique. When I_{cry} is close to 1, it is assumed that the crystallites represent monocrystalline units, whereas greater values of I_{cry} indicate polycrystalline nature [41].

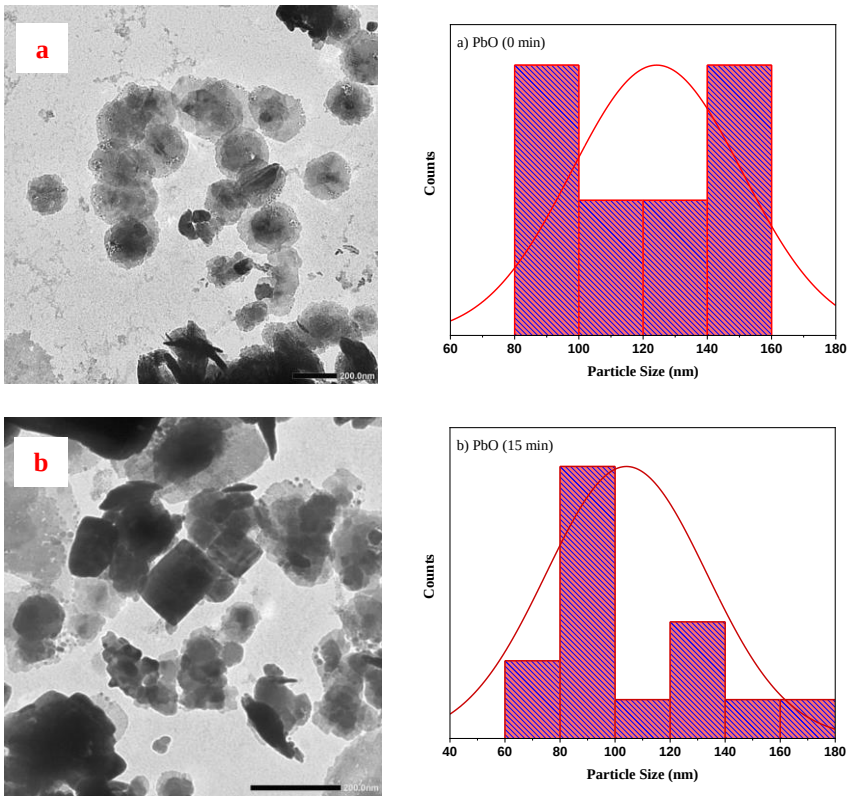

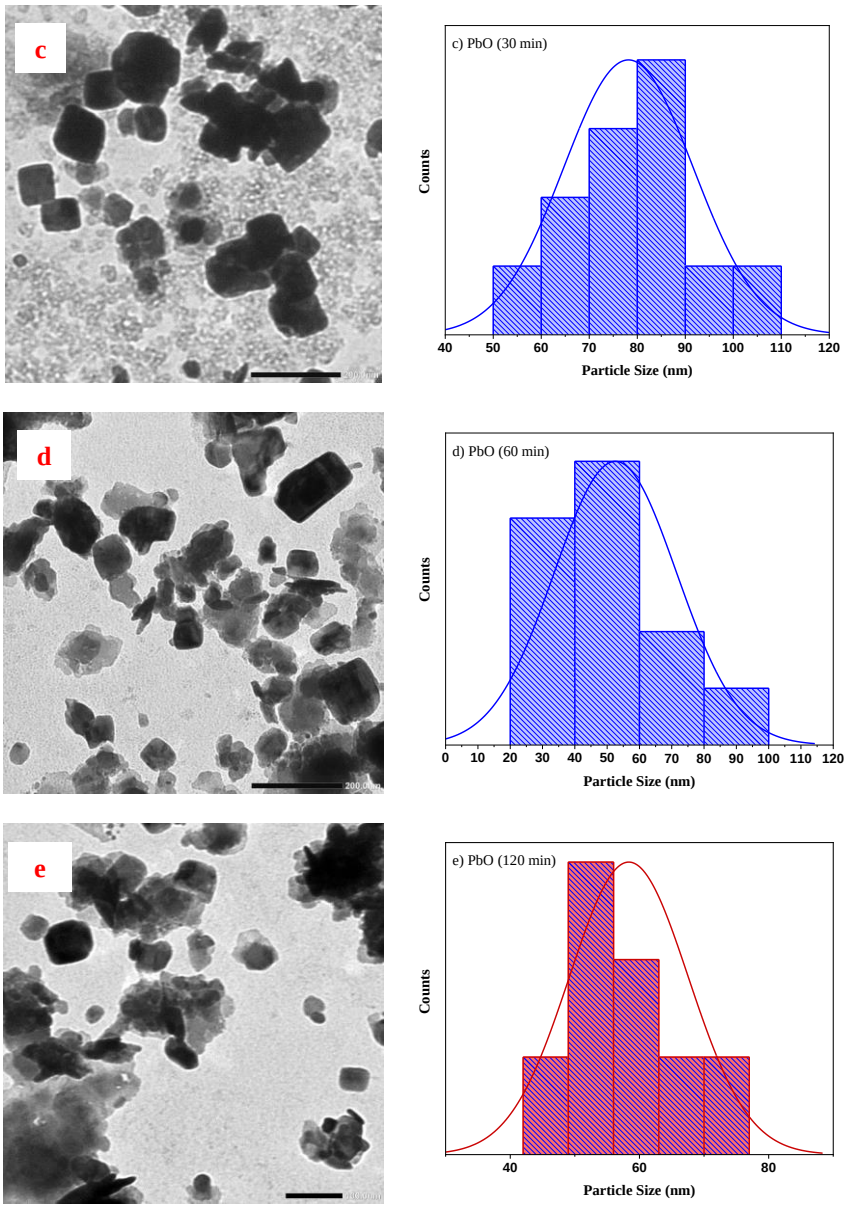

Fig. 2. TEM micrographs with the corresponding size histograms for (a) PbO(Bulk), and PbO particles milled for (b) 15 minutes, (c) 30 minutes,(d) 60 minutes and (e) 120 minutes.

The calculated values of the crystallinity index of synthesized PbO particles were listed in Table 2. The results implied a monocrystalline type for PbO bulk and nanoparticles milled for 30 and 60 minutes, whereas PbO particles milled for 15 minutes revealed a polycrystalline nature, which was already confirmed by XRD results.

According to the results of PbO characterization, PbO particles milled for 15 minutes did not reach the nano-size; additionally, PbO particles milled for 120 minutes exhibited agglomeration and a larger nano-size than those milled previously (60 minutes). Accordingly, PbO particles milled for 30 and 60 minutes denoted PbO(A) and PbO(B), respectively, were the best candidates for this study due to less agglomeration and distinguishable nano sizes.

The grinding method has indeed been successful in producing nano-sized particles and has an edge over other procedures in terms of yield. The selected nano-produced PbO will be incorporated into the polystyrene to investigate the effect of PbO nano-size on the X-ray attenuation ability of the composite. In addition, the fact that nano PbO has a larger surface-to-volume ratio will affect and improve the attenuation ability of the composite having a smaller size of nano PbO.

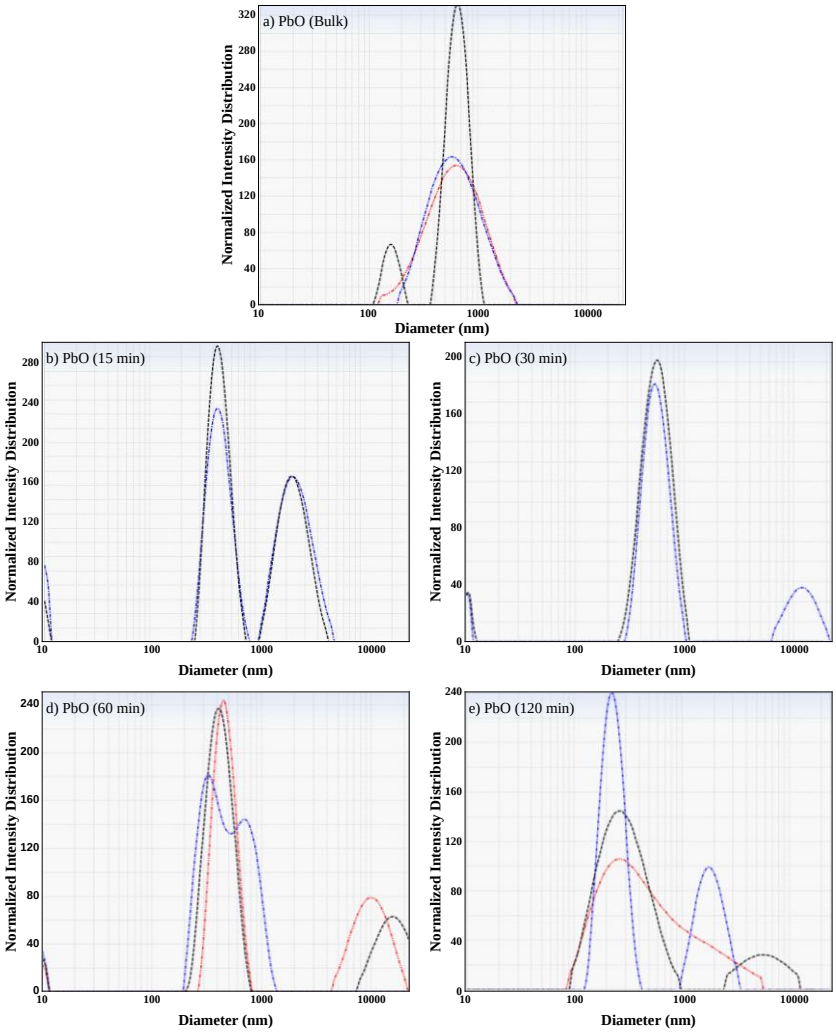

Fig. 3. DLS spectra of PbO particles milled for (a) 0, (b) 15, (c) 30,(d) 60 and (e) 120 minutes.

Table 2. Particle sizes measured by XRD and TEM, and the crystallinity index I_{cry}.

Milling Time (minutes)	Mean size (XRD) D (nm)	Mean size (TEM) D_p (nm)	Crystallinity I_{cry}
0	147.20	124.26	0.84
15	94.40	100.87	1.07
30	78.40	78.17	1.00
60	54.80	52.56	0.96
120	55.30	58.36	1.06

3.1.4. FTIR

The chemical bonding of PbO particles was investigated using FTIR, and the spectra of PbO bulk, PbO(A) and PbO(B) are illustrated in Figs. 4(a)-(c). The appearance of the transmission band at 682 cm^{-1} reflects the presence of an asymmetric bending vibration of the Pb-O-Pb bond [40]. The spectrum of each sample shows other bands in the region 4000-1000 cm^{-1} which usually refer to organic compounds. Broadband around 1400 cm^{-1} refers to -OH bending vibration. The infrared peak at 2343 cm^{-1} is generally related to C=O stretching vibration modes that refer to the contribution of CO_2 dissolution from the air [12, 41]. The PbO characteristic bands are similar to those found in previous studies in which PbO nanoparticles were prepared using various methods such as chemical synthesis [41, 42] and laser ablation [43].

Udvardi et al. [44] and Meyers et al. [45] studied the effect of particle size with a micrometric scale on the FTIR spectra (intensity, area bands, reflectance…). They demonstrated that for the regions where the spectral features are attributed to fundamental molecular vibrations or a combination of bands, a decrease in particle size implies an increase in the overall reflectivity and an increase in the bands in spectral contrast, as shown in Fig. 4. Indeed, the intensity of the PbO band is lower for the PbO (Bulk) compared to the band intensity of the nanoparticles PbO (A) and PbO (B). As the particle size decreases, the incident radiation covers a greater fractional surface area and passes through less of the absorbing medium, resulting in an increase in overall reflectivity and an increase in spectral contrast transmittance bands. The opposite trend is observed in some of the features below 3000 cm^{-1} in which the spectral contrast decreased as particle size decreased which is the case of H-OH bending vibration in the FTIR spectra of Fig. 4. For these bands, the absorption at the center of the band is greater due to a higher absorption coefficient.

3.2. PS/PbO characterization

The results of experimental characterization tests on PS/PbO composites are discussed in the following section.

3.2.1. XRD for PS/PbO composites

Figures 5(a) and 6(a) depict the experimental and refined XRD patterns of the polystyrene sample. The refinement assured the pure form of the polymer with $(C_8H_8)_n$ chemical formula, with reliable goodness-of-fit value (χ^2 approaching unity). The polymer's two most pronounced peaks are situated at 2θ = 9.69° and 19.38°. The presence of peaks at 2θ=9.69° implies amorphous material, whereas peaks at 19.38° indicate crystalline polymer material [46].

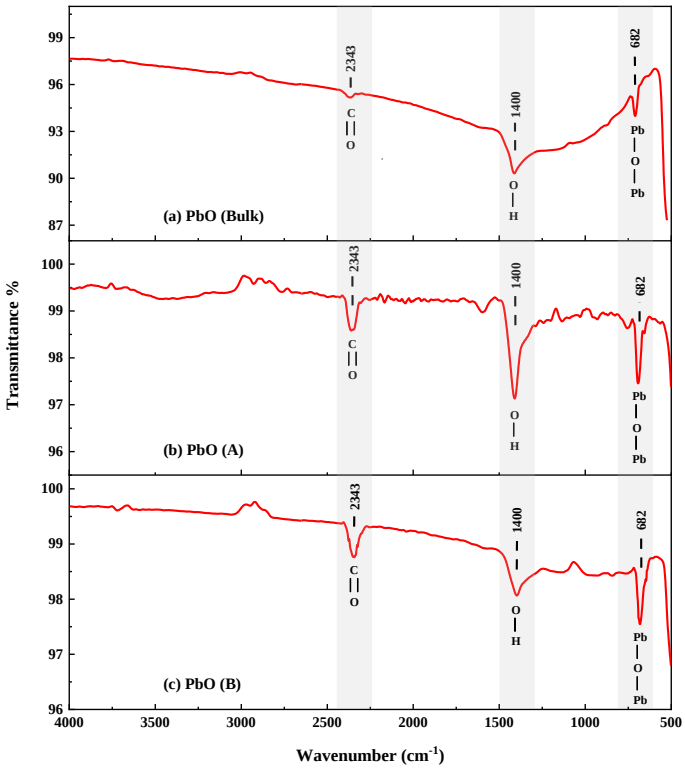

Fig. 4. FTIR spectra for (a) PbO (Bulk), (b) PbO(A) and (c) PbO(B).

The experimental and refined XRD patterns of PS with bulk PbO are depicted in Figs. 5 and 6(b) and (c). In addition to the typical peaks of PS (9.69° and 19.38°), it revealed the orthorhombic phase (β-PbO) peaks with minor tetragonal peaks (α-PbO) that were previously discussed in paragraph 3.1. The addition of PbO filler has resulted in an increase in the intensity of PbO peaks as well as a decrease in the strength of the PS characteristic peaks. The changes in the phase percentages of PS, β-PbO and α-PbO, extracted from the refinements, are graphically demonstrated in Fig. 7(a). Considerably, the PS% decreased with the addition of the PbO filler, which originally contains both β-PbO and α-PbO phases, which witnessed increased percentages.

In regard to nanocomposites PS/PbO(A) and PS/PbO(B), their experimental and refined XRD patterns, are plotted in Figs. 5 and 6 (d)-(g), revealed peaks of the tetragonal phase of α-PbO, as described in paragraph 3.1, in addition to the characteristic peaks of PS. When the weight percentage of PbO increased, the intensity of PbO peaks increased while the intensity of PS characteristic peaks declined. This follows the variations of the phase percentages of PS and α-PbO with the addition of the PbO fillers, as plotted in Figs. 7 (b) and (c). Moreover, the addition of the fillers to the PS polymer resulted in a reduction of the amorphous nature and enhancement of the crystalline nature. This is detected from the XRD patterns, where the broadness of the peaks related to PS decreased as well as their intensity with the addition of the fillers. Moreover, sharp and narrow peaks of crystalline PbO structure emerged in the patterns, further enhancing the crystalline nature of the nanocomposites.

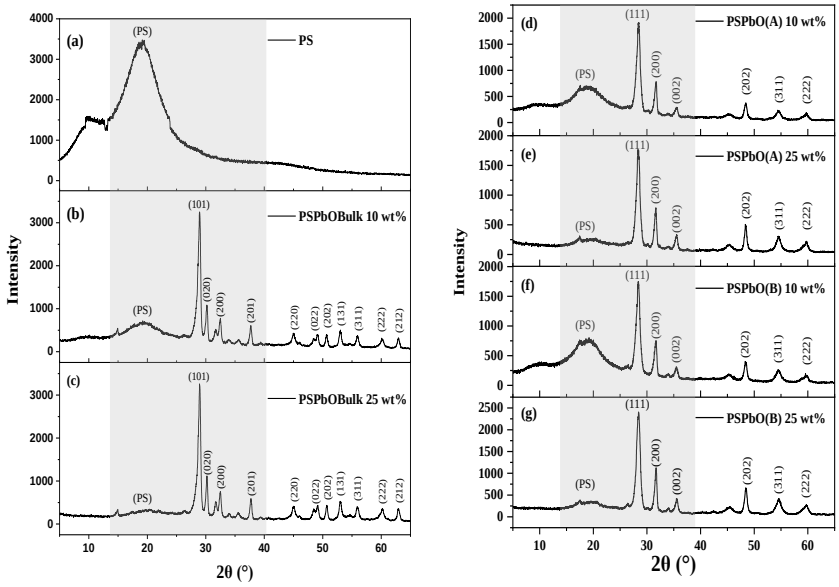

Fig. 5. The X-ray diffraction patterns of (a) PS, (b) PS/PbO Bulk 10 wt%, (c) PS/PbO Bulk 25 wt%, (d) PS/PbO(A) 10 wt%, (e) PS/PbO(A) 25 wt%, (f) PS/PbO(B) 10 wt%, and (g) PS/PbO(B) 25 wt%.

The characteristic peaks of PbO for both orthorhombic and tetragonal phases were not altered, and neither were the characteristic peaks of PS in the produced composites. The d-spacing values computed from the PS peak remained fairly stable (around 4.5 Å), indicating the absence of any chemical interaction and reflecting the adsorption of the metal oxide within the polymer matrix [47].

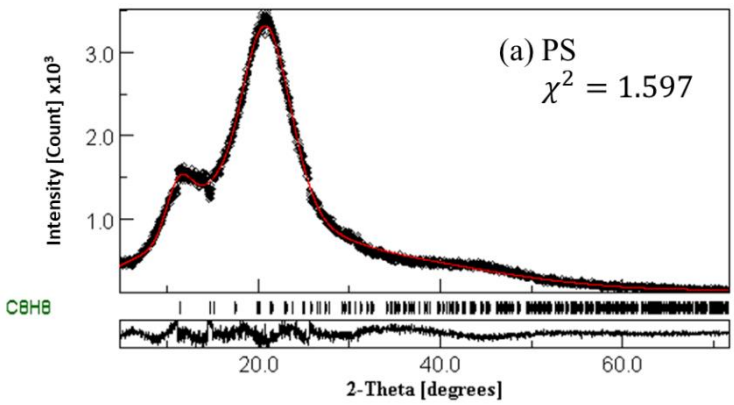

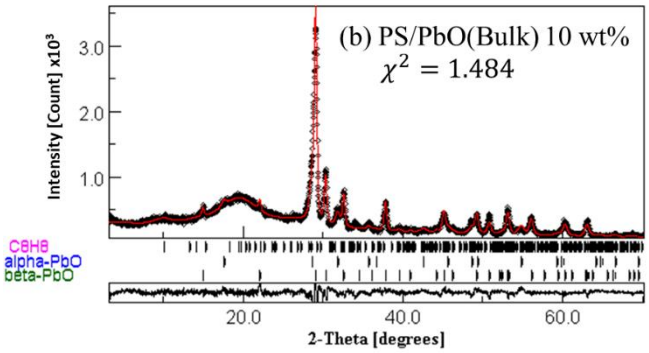
(b) PS/PbO(Bulk) 10 wt%
$\chi^2 = 1.484$
Intensity [Count] x10³
3.0
2.0
1.0
C8H8
alpha-PbO
beta-PbO
20.0
40.0
60.0
2-Theta [degrees]

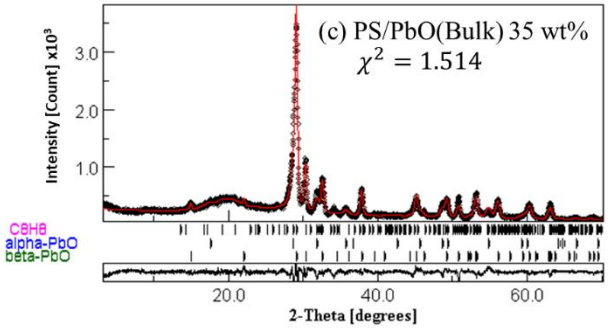
(c) PS/PbO(Bulk) 35 wt%
$\chi^2 = 1.514$
Intensity [Count] x10³
3.0
2.0
1.0
C8H8
alpha-PbO
beta-PbO
20.0
40.0
60.0
2-Theta [degrees]

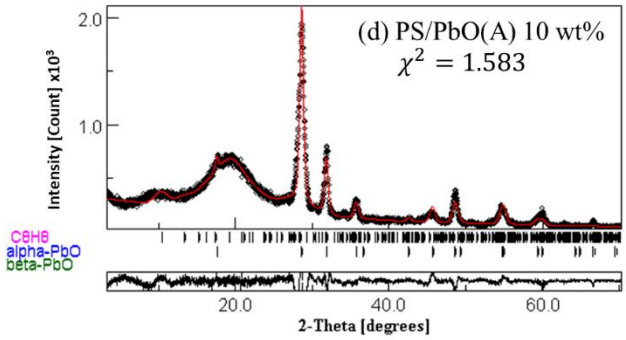
(d) PS/PbO(A) 10 wt%
$\chi^2 = 1.583$
Intensity [Count] x10³
2.0
1.0
C8H8
alpha-PbO
beta-PbO
20.0
40.0
60.0
2-Theta [degrees]

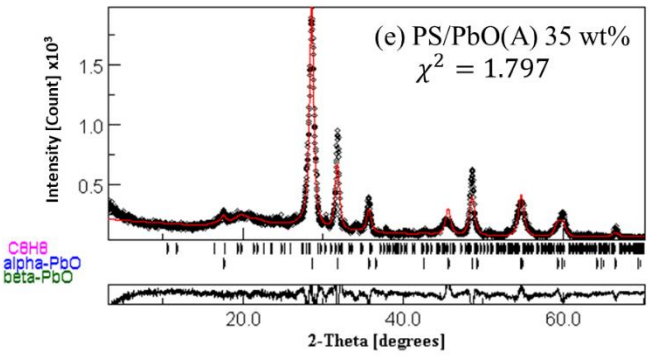
(e) PS/PbO(A) 35 wt%
$\chi^2 = 1.797$
Intensity [Count] x10³
1.5
1.0
0.5
C8H8
alpha-PbO
beta-PbO
20.0
40.0
60.0
2-Theta [degrees]

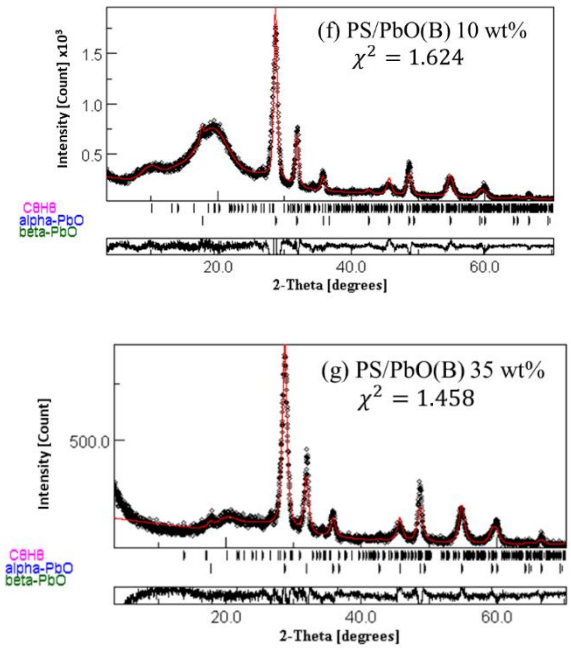

Fig. 6. The Reitveld refinements of some selected PS/PbO samples.

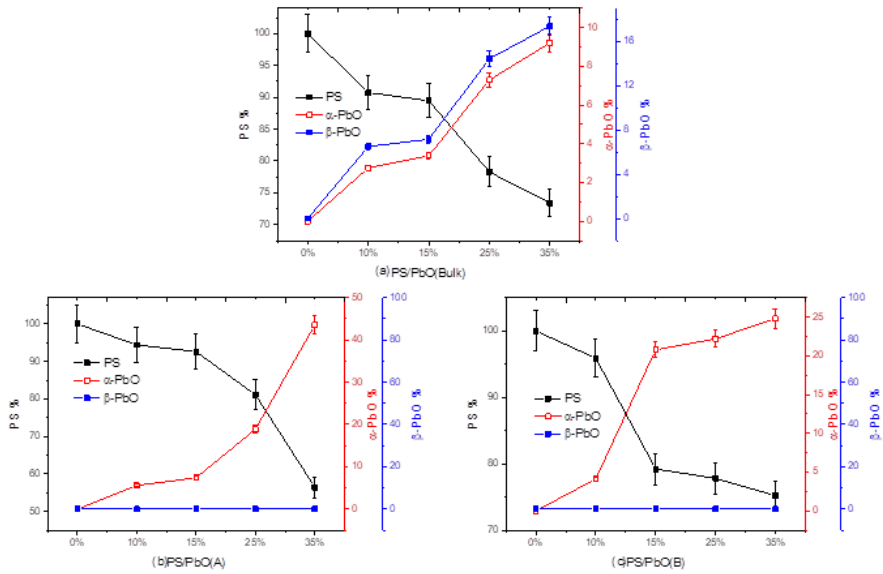

Fig. 7. The variations in the phase percentages of PS, β-PbO and α-PbO.

3.2.2. Thermal properties of the PS/PbO composite

Following is the discussion part of the TGA and DSC-based thermal property analysis of PS/PbO composites.

3.2.2.1. TG analysis

Thermogravimetric analysis (TGA) was used to investigate the thermal degradation of PS and PS/PbO composites. Figures 8(a)-(c) illustrated the obtained TGA curves for the investigated PS/PbO composites, while their corresponding derivatives (DTA) are shown in the insets of Figs. 8(a)-(c). The TGA curves for all the prepared samples revealed a single degradation step [19], and T_{ini} and $T_{50\%}$ temperatures, which correspond to a 5% and 50% weight loss of the investigated sample, were calculated and summarized in Table 3. PS decomposition was initiated at 379 °C and continued until complete decomposition occurred at 470 °C, leaving a residual mass of 0.30%. Similar results were obtained by Kreuts et al. [17] and Dominguini et al. [48], indicating that the thermal decomposition of PS began at 387 and 380 °C, respectively.

As expected, the thermal stability was improved with increasing PbO content in the composite. T_{ini} and $T_{50\%}$ of PS/PbO(Bulk) increased when the filler load increased to 15 and 25 wt%, and then decreased with further load increase. This finding might be explained by the presence of agglomerates in composites with a high concentration of PbO (Bulk), which reduces the thermal stability of the polymeric matrix, and hence decreases T_{ini} and $T_{50\%}$ [49]. Otherwise, as shown in Figs. 8(b)-(c), T_{ini} and $T_{50\%}$ of PS/PbO(A) and PS/PbO(B) nanocomposites increased with increasing filler loads in the PS matrix, owing to fine dispersion and less agglomeration of nanoparticles PbO(A) and PbO(B). The addition of 35 wt% of PbO filler with nano-size (A) increased the values of T_{ini} and $T_{50\%}$ from 379 and 413.9 °C to 384.45 and 420.10 °C, respectively, whereas the addition of 35 wt% of PbO filler with nano-size (B) increased T_{ini} and $T_{50\%}$ values to 384.60 and 421.75 °C, respectively. Such shifts are unambiguous indicators of the enhanced thermal stability of polymer nanocomposites related to the incorporation of PbO nanoparticles into the polymer matrix. PbO nanoparticles are inorganic non-degradable material; decreasing particle size increases surface areas and subsequently decreases the chain mobility when dispersed in a polymer matrix, and prevents out-diffusion of the volatile decomposition products, resulting in a delay in the thermal degradation of the polymer [20, 50-52].

After reaching 470 °C, there are no residues left for the PS [21], and the final residual mass percentage for PS/PbO composites at 600°C were calculated and listed in Table 3. The results indicated a systematic increase in the residual mass percentage with increasing filler load for all the PS/PbO composites. Furthermore, the residual mass percentage increased with decreasing particle nano size and showed an increment of 36.4 % for PS/PbO(B) 35wt% over that of PS/PbO(Bulk) 35wt%. Such results refer to the fine dispersions of nanofillers and the homogeneity of the composites.

Decomposition temperatures (T_p) and decomposition rates for PS and PS/PbO composites, indicated in Table 3, were obtained from the differential thermal analysis curves DTA. The enlargement of the DTA curves is depicted as insets of Figs. 8(a)-(c) for PS and PS/PbO composites. The presence of a single peak in DTA thermograms confirms that PS and PS/PbO composites underwent a single degradation step. All studied samples had a similar degradation process. The decomposition temperatures T_p for PS and PS/PbO composites were approximately 416 °C, with a very slight increase with increasing PbO loads. In contrast, the decomposition rate of the PS/PbO composite is lower than that for PS and decreases as the weight percent of PbO increases, as well as, decreasing PbO particle size. The lowest decomposition rate was obtained for the composite with the highest

weight fraction and the smallest particle size, PS/PbO(B) 35wt%, with a 35% decrement compared to PS.

Table 3. Degradation temperatures and residual mass percentages of PS and PS/PbO composite.

Sample	wt%	TGA results			DTA results	
		T_{ini} (°C)	$T_{50\%}$ (°C)	Residual mass %	Decomp. temperature T_p (°C)	Decomp. rate (%/°C)
PS	0	379.00	413.90	0.30	416.27	3.06
PS/PbO (Bulk)	10	382.50	415.70	9.13	416.30	2.72
	15	383.40	417.60	15.33	416.33	2.63
	25	383.20	419.70	22.16	416.34	2.26
	35	382.00	418.00	22.87	416.40	2.31
PS/PbO (A)	10	378.00	415.45	9.04	416.32	2.78
	15	381.00	414.40	9.04	416.35	2.64
	25	381.40	416.90	17.90	416.37	2.47
	35	384.45	420.10	29.56	416.47	2.11
PS/PbO (B)	10	381.25	415.35	6.30	416.33	2.95
	15	381.65	417.00	9.90	416.37	2.59
	25	384.40	419.70	26.40	416.37	2.19
	35	384.60	421.75	31.20	416.50	1.93

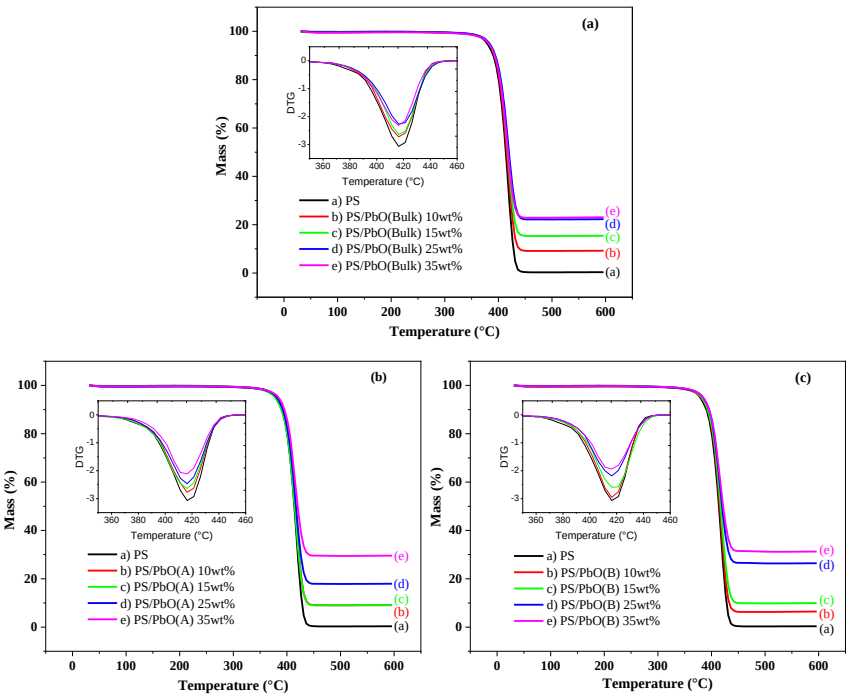

Fig. 8. TGA curves for PS/PbO composites with filler (a) PbO(Bulk), (b) PbO(A), and (c) PbO(B). The insets represent the DTA curves for the same group of samples.

This occurs as a result of the physical interaction between the polymer and PbO layers. Furthermore, due to their high thermal conductivity and high heat capacity, PbO nanoparticles acted as effective heat sinks that counteracted the amount of heat that the PS polymer backbone could acquire, leading to a reduced rate of degradation and an enhancement in the thermal stability of the composites [51, 52]. Since the DTA profiles of nanocomposites are identical to those of pure PS, it is argued that there is no substantial difference in the degradation mechanism; nevertheless, the processes of degradation are delayed.

Kinetic analysis of the thermal degradation process for pure PS and PS/PbO nanocomposites has been performed to deeply comprehend the degradation behavior of composites in contrast to pure PS. The activation energy, *E*, can be calculated using Eq. (2) based on the approximations given by Horowitz and Metzger [53].

$$\ln\left[\ln\left(\frac{m}{m_o}\right)\right] = -\frac{E}{R}\left(\frac{1}{T}\right) + A \qquad (2)$$

where m and m_o are the masses of the sample at a given temperature and the initial sample mass, respectively, R is the ideal gas constant, and A is a constant.

For this purpose, TGA data of the investigated PS/PbO nanocomposites were utilized. Thus, the plots of ln[ln(*m/mo*)] versus 1/*T* depicted in Figs. 6(a)-(c) yield a straight line whose slope is proportional to the activation energy. The lines obtained at a different weight fraction of PbO are observed to be roughly parallel to one another and the correlation coefficient of the linearity for the calculation of each activation energy is larger than 0.99.

The obtained kinetic parameter values *E/R* and *A* are enlisted in Table 4. Similar to the degradation rate, the activation energy *E*, for PS/PbO composites showed a decrease with increasing filler weight percentage. Polymer degradation is linked to the presence of weak links, such as head-to-head, hydroperoxy, and peroxy structures, within polymer composites that readily break down at extremely low temperatures to create radicals that contribute to the subsequent degradation process at elevated temperatures.

At higher degradation temperatures, meanwhile, char production may significantly contribute to the reported improved thermal stability via the "cage effect" phenomenon, in which gaseous molecules generated during thermal decomposition are trapped within the solid inorganic-organic network [54].

For PS, tertiary carbons where polystyrly radicals are bound to the polymer main chain have low bond energy. In addition, there is just one C-H bond, whereas carbon atoms in other positions along the main chain possess many C-H bonds. Because the binding energy of C-H is 414 kJ/mol and the bond energy of C-C is 348 kJ/mol, the tertiary carbon position has the lowest bond energy and so releases the polystyrly free radical. Incorporating PbO nanoparticles into the polymer matrix may eventually act as scavengers of the polystyrly free radicals, and therefore delaying the thermal degradation of the polymer [55].

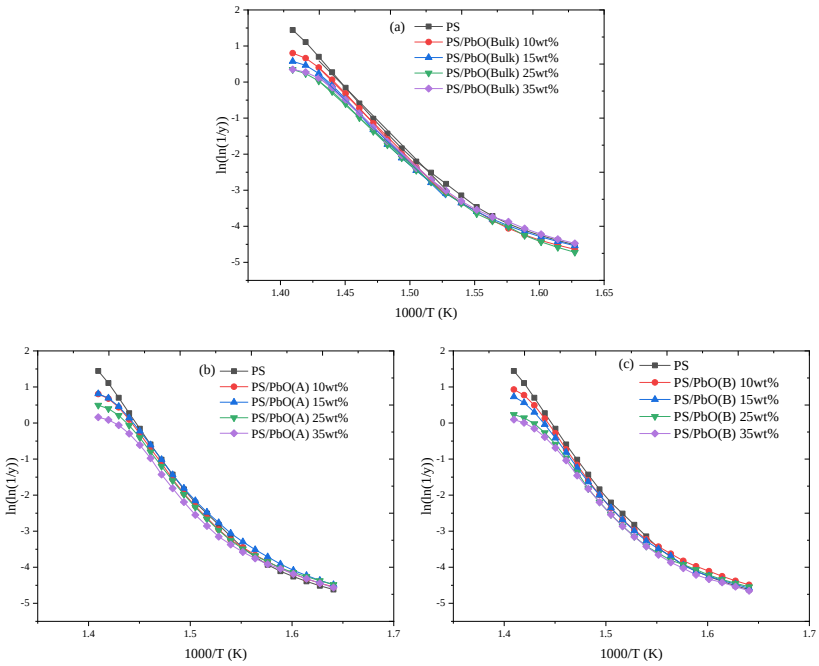

Fig. 9. Ln(lnm/m$_0$) vs. 1000/T of PS/Pb composites.

Table 4. Kinetic parameters and activation energies calculated for the PS and PS/PbO composites.

Sample	wt%	ln[ln(*m/mo*)] vs. 1/*T*		
		-E/R	*A*	*E* (kJ/mol)
PS	0	-36.92	53.36	306.91
PS/PbO(Bulk)	10	-36.05	51.93	299.73
	15	-34.86	50.04	289.79
	25	-32.46	46.44	269.88
	35	-32.96	47.27	274.05
PS/PbO(A)	10	-35.15	50.64	292.24
	15	-34.84	50.28	289.66
	25	-34.65	49.82	288.11
	35	-33.41	47.79	277.78
PS/PbO(B)	10	-36.36	53.83	302.26
	15	-35.03	50.36	291.24
	25	-34.86	49.93	289.79
	35	-33.20	47.43	276.04

3.2.2.2. DSC analysis

Differential scanning calorimetry (DSC) was performed for the PS and the PS/PbO composites. Polystyrene is known to be an amorphous polymer. As the temperature increases, amorphous and semicrystalline polymers go through the glass transition (T_g). Amorphous polymers do not exhibit other phase transitions; however, semicrystalline polymers undergo crystallization and melting. Previous studies investigated the glass transition temperature of PS and PS composites. Pierella et

al. [56] found that the T_g of PS is around 100°C, whereas Rieger et al. [57] reported that T_g of PS scattered around 107°C. Farha et al. [19] discovered that PS/ZnO glass transition temperature fluctuated between 90 and 100°C. The result of the DSC heating thermogram for the PS is displayed in Fig. 10. An abrupt and linear rise in the signal before quickly leveling out is shown in the graph, indicating a single glass transition peak (T_g) for the PS at 105.28 °C [50, 58, 59]. Figures 11(a)-(c) illustrate the DSC heating thermograms for PS/PbO composites, which also revealed a single glass transition. The T_g values of the PS/PbO composites listed in Table 5 fluctuated around that of PS, with PS/PbO(B) 35wt% showing a good enhancement with an increment of 2.17 % over that of PS. Moreover, a very modest endothermic peak was detected at a low-temperature range (close to 100 °C) before T_g of PS, which is associated with water vapor [19, 60-62].

In the literature review, several parameters were employed to analyse the thermal properties of various composites; also, the studied metal oxide fillers were distinct from PbO. However, Table 6 displays the results of both the literature review and the current investigation.

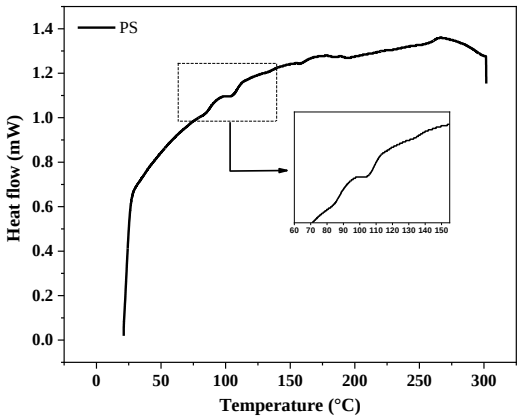

Fig. 10. DSC heating curves for Polystyrene showing the glass transition.

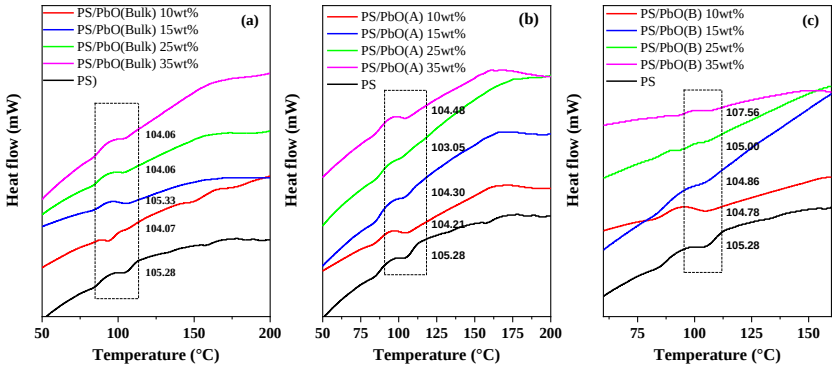

Fig. 11. DSC heating curves for
(a) PS/PbO bulk, (b) PS/PbO(A), and (c) PS/PbO(B).

Table 5. DSC results for pure PS and PS/PbO composites.

Sample	wt%	DSC results		
		T_{Onset} (°C)	T_g (°C)	T_{Endset} (°C)
PS	0	97.59	105.28	112.37
PS/PbO(Bulk)	10	101.47	104.07	106.54
	15	98.60	105.33	110.73
	25	97.00	104.06	109.00
	35	99.00	104.06	107.00
PS/PbO(A)	10	99.76	104.21	108.18
	15	98.11	104.3	112.49
	25	95.13	103.05	110.18
	35	99.54	104.48	106.48
PS/PbO(B)	10	97.16	104.78	111.74
	15	98.55	104.86	108.84
	25	100.63	105.00	108.51
	35	98.77	107.56	113.66

Table 6. Comparison with the results obtained from the literature review.

Researchers	Composites	Thermal analysis results
Ahmad et al. [18]	WPS-rGO-CuO	The weight losses at 250-400°C are 73.36, 22.02, and 20.01%, for WPS, WPS-rGO-CuO:2%, and WPS-rGO-CuO:15%.
Farha et al. [19]	PS/ZnO	Thermal degradation delay of 10°C for PS/ZnO 1 wt%.
Karimabad et al. [20]	PS-SiO2	The thermal decomposition of the PS-SiO2 composite is shifted towards a higher temperature (370 °C).
Suresh et al. [21]	PS/ Ni-Al LDH	For PS/ Ni-Al LDH 7 wt%, the glass transition T_g is 4.3 °C higher than that of PS and the degradation temperature T_d is enhanced by 27.4 °C.
El Gamal et al. [22]	PbO/PVC/PMMA	Degradation temperatures of PS/PMMA blend are: T_{onset} = 268.9, $T_{10\%}$ = 280.6 and $T_{50\%}$ = 361.9 °C. For nanocomposite with 2 wt% of PbO load, T_{onset} = 280.5, $T_{10\%}$ = 300.8 and $T_{50\%}$ = 377.9 °C.
Mahmoud et al. [23]	HDPE/PbO	Incorporating PbO bulk increased the values of T_{ini} and $T_{50\%}$ by 15.7% and 3.6%, respectively, whereas the increment is 18.2 and 4.1% for HDPE/PbO NP.
This study	PS/PbO	PS/PbO having 35 wt% of the lowest nano size (B) of PbO exhibited an increment of 0.5% for characteristic temperatures T_{ini} and $T_{50\%}$ (384,6 and 421.75 °C), 36.4 % of the residual mass percentage, and 2.17% of the glass transition temperature (T_g=107.56 °C).

4. Conclusions

PbO nanoparticles were successfully synthesized via high-speed planetary ball milling and then incorporated into the PS matrix via melt mixing and compressing moulding techniques for the synthesis of PS/PbO composites.

The XRD analysis revealed that bulk PbO has a monocrystalline orthorhombic structure, PbO particles milled for 15 minutes have a polycrystalline structure (Orthorhombic and Litharge), and all other milled PbO particles have a monocrystalline lighterage structure, indicating a phase transition for nanoparticles from β-PbO to α-PbO with increasing milling time.

The TEM results indicated that the particle sizes of PbO were consistent with those determined by XRD, whereas the DLS results indicated a moderate aggregation spectrum for PbO particles milled for 15 and 120 minutes and a low aggregate spectrum for PbO particles milled for 30 and 60 minutes. XRD results of PS/PbO composites showed that the phase percentage of PS and α-PbO decreased, with increasing PbO contents. Furthermore, the thermal properties of the composites were influenced by the incorporation of the PbO particles in the PS matrix. TGA analysis revealed that the characteristic temperatures (T_{ini} and $T_{50\%}$) and the residual mass percentage of nanocomposites increased with increasing the load and decreasing the size of PbO particles.

A Further advanced investigation, through differential and kinetics thermal analysis of the degradation process of the composites, revealed a decrease in the decomposition rate and an enhancement in the activation energy with increasing PbO load and decreasing particle size.

The prepared PS/PbO will be examined for X-ray shielding purposes. The investigation of the thermal and mechanical properties was crucial for composite characterization. Thermal analysis results were convenient since the incorporation of PbO with different sizes has improved the thermal properties of PS and did not have a detrimental effect.

Nomenclatures

D	Average crystallite size calculated from XRD
D_p	Average crystallite size calculated from TEM
E	Oxygen diffusion activation energy
I_{cry}	Crystallinity
T_{ini}	Temperature which corresponds to a 5% weight loss of the investigated sample
$T_{50\%}$	Temperature which corresponds to a 50% weight loss of the investigated sample
T_g	Temperature which corresponds to a glass transition
T_{Onset}	Temperature where glass transition starts
T_{Endset}	Temperature where glass transition ends

References

1. Selvi, J.; Parthasarathy, V.; Mahalakshmi, S.; Anbarasan, R.; Daramola, M.O.; and Kumar, P. S. (2020). Optical, electrical, mechanical, and thermal

properties and non-isothermal decomposition behavior of poly(vinyl alcohol)-ZnO nanocomposites. *Iranian Polymer Journal*, 29, 411-422.

2. Nazaripour, E.; Mousazadeh, F.; Moghadam, M.D.; Najafi, K.; Borhani, F.; Sarani, M.; Ghasemi, M.; Rahdar, A.; Iravani, S.; and Khatami, M. (2021). Biosynthesis of lead oxide and cerium oxide nanoparticles and their cytotoxic activities against colon cancer cell line. *Inorganic Chemistry Communications*, 131, 108800.
3. Alsayed, Z.; Awad, R.; and Badawi, M.S. (2020). Thermo-mechanical properties of high density polyethylene with zinc oxide as filler. *Iranian Polymer Journal*, 29, 309-320.
4. Delides, C. G. (2016). Everyday Life Applications of Polymer Nanocomposites. *Conference: e-RA 11*. Athens, Greece, 1-8.
5. Hassan, T.; Abdul Salam, Khan, A.; Khan, S.; Khanzada, H.; Wasim, M.; Khan, M.Q.; and Kim, I. S. (2021). *Journal of Polymer Research*, 28, 36.
6. More, C.V.; Alsayed, Z.; and Badawi, M.S. (2021). Polymeric composite materials for radiation shielding: a review. *Environmental Chemistry Letters*, 19, 2057-2090.
7. Alsayed, Z.; Badawi, M.S.; Awad, R.; Thabet, A.A.; and El-Khatib, A. M. (2019). Study of some γ-ray attenuation parameters for new shielding materials composed of nano ZnO blended with high density polyethylene. *Nuclear Technology and Radiation Protection*, 34(4), 342-352.
8. Alsayed, Z.; Badawi, M.S.; Awad, R.; El-Khatib, A.M.; and Thabet, A.A. (2020). Investigation of γ-ray attenuation coefficients, effective atomic number and electron density for ZnO/HDPE composite. *Physica Scripta*, 95(8), 085301.
9. Yabagi, J. A.; Kimpa, M. I.; Muhammad, B. L.; Hamzah, M. Q.; Abdul Kadir, H. K.; and Agam, M. A. (2020). The effect of silver particles on the synthesis and characterization of polystyrene/Silver (Ps/Ag) nanocomposites for carbonaceous materials. *International Journal of Nanoelectronics and Materials*, 13(2), 263-282.
10. Chen, B.; and Torkelsonk, J.M. (2021). Rigid amorphous fraction and crystallinity in cold-crystallized syndiotactic polystyrene: Characterization by differential scanning calorimetry. *Polymer*, 230, 124044.
11. Alharshan, G. A.; Aloraini, D. A.; Abd Elzaher, M.; Badawi, M.S.; Alabsy, M.T.; Abbas, M.I.; El-and khatib, A.M. (2020). A comparative study between nano-cadmmium oxide and lead oxide reinforced in high density polyethylene as gamma rays shielding composites. *Nuclear Technology & Radiation Protection*, 35(1), 42-49.
12. Bratovic, A. (2020). *Lead Chemistry book*. IntechOpen.
13. Joshi, G. M.; Khadeer Pasha, S.K.; and Chidambaram K. (2013). Modified PVA moiety with PbO as humidity sensor. *Composite Interfaces*, 20(5), 331-341.
14. Khadheer Pasha, S. K.; Deshmukh, K.; Ahamed, M. B.; Chidambaram, K.; Mohanapriya, M.K.; and Arunai Nambi Raj, N. (2015). Investigation of microstructure, morphology, mechanical, and dielectric properties of PVA/PbO Nanocomposites, *Advances in Polymer Technology*, 36(3), 21616-21626.
15. Kalkornsuranee, E.; Intom, S.; Lehman, N.; Johns, J.; Kothan, S.; Sengloyluan, K.; Chaiphaksa, W.; and Kaewkhao, J. (2020). Mechanical and gamma

radiation shielding properties of natural rubber composites: effects of bismuth oxide (Bi2O3) and lead oxide (PbO). *Materials Research Innovations*, 26(1), 8-15.

16. Muhammad, W.; Khan, M. A.; Nazira, M.; Siddiquah, A.; Mushtaq, S.; Hashmi, S.S.; and Abbasia, B.H. (2019). Papaver somniferum L. mediated novel bioinspired lead oxide (PbO) and iron oxide (Fe2O3) nanoparticles: In-vitro biological applications, biocompatibility and their potential towards HepG2 cell line. *Materials Science & Engineering: C*, 3, 109740.
17. Kreutz, J. C.; Souza, P.R.; Benetti, V.P.; Freitas, A.R.; Bittencourt, P.R.S.; and Gaffo, L. (2021). Mechanical and thermal properties of polystyrene and medium density fiberboard composites, *Polímeros*, 31(2), 2021013.
18. Ahmad, W.; Ahmad, Q.; Yaseen, M.; Ahmad, I.; Hussain, F.; Jan, B.M.; Ikram, R.; Stylianakis, M.M.; and Kenanakis, G. (2021). Development of Waste Polystyrene-Based Copper Oxide/Reduced Graphene Oxide Composites and Their Mechanical, Electrical and Thermal Properties. *Nanomaterials*, 11(9), 2372.
19. Farha, A. H.; Al Naim, A. F.; and Mansour, S. A. (2020). Thermal Degradation of Polystyrene (PS) Nanocomposites Loaded with Sol Gel-Synthesized ZnO Nanorods. *Polymers*, 12(9), 1935.
20. Karimabad, A.E.B.; Moghadam, L.N.; Niasari, M.S.; and Bagheri, S. (2019). Synthesis of SiO2 Nanocrystals by Two Approaches and Their Application in Photocatalytic Degradation and Flame Retardant Polymeric Nanocomposite. *Journal of Inorganic and Organometallic Polymers and Materials*, 29, 378-389.
21. Suresh K.; Kumar, M.; Pugazhenthi, G.; and Uppaluri, R. (2017). Enhanced mechanical and thermal properties of polystyrene (PS) nanocomposites prepared using organo-functionalized Ni-Al layered double hydroxide (LDH) via melt intercalation technique. *Journal of Science: Advanced Materials and Devices*, 2, 245-254.
22. El-Gamal, S.; and Elsayed, M. (2020). Synthesis, structural, thermal, mechanical, and nano-scale free volume properties of novel PbO/PVC/PMMA nanocomposites. *Polymer*, 206, 122911.
23. Mahmoud, M.E.; El-Khatib, A.M.; El-Sharkawy, R.M.; Rashad, A.R.; Badawi, M.S.; and Gepreel, M.A. (2019). Design and testing of high-density polyethylene nanocomposites filled with lead oxide micro- and nano-particles: Mechanical, thermal, and morphological properties. *Journal of Applied Polymer Science*, 136(31), 47812.
24. Shakfa, Z.M.; Hannora, A.E.; and Sherif, M.M. (2015). Preparation of Lead-Polymer Nano composite For Nuclear Shielding Applications. *International Journal for Research in Applied Science and Engineering Technology*, 3, 1046-1049.
25. Torabi, M.; Razavi, S.H.; and Sanjabi, S. (2011). Electrochemical evaluation of PbO nanoparticles as anode for lithium ion batteries. *IJE Transactions B: Applications*, 24(4), 351-355.
26. Khalil, A. T.; Ovais, M.; Ullah, I.; Ali, M.; Jan, S.A.; Shinwari, Z.K.; and Maaza, M. (2020). Bioinspired synthesis of pure massicot phase lead oxide nanoparticles and assessment of their biocompatibility, cytotoxicity and in-vitro biological properties. *Arabian Journal of Chemistry*, 13(1), 9-46.

27. Ng, S. H.; Wang, J.; Konstantinov, K.; Wexler, D.; Chen, J.;and Liu, H.K. (2006). Spray pyrolyzed PbO-carbon nanocomposites as anode for lithium-ion ed PbO-carbon nanocomposites as anode for lithium-ion batteries. *Journal of the Electrochemical Society*, 153(4), 787-793.
28. Khalil, A.T.; Ovais, M.; Ullah, I.; Ali, M.; Jan, S.A.; Shinwari, and Z.K.; Maaza, M. (2020). Bioinspired synthesis of pure massicot phase lead oxide nanoparticles and assessment of their biocompatibility, cytotoxicity and in-vitro biological properties. *Arabian Journal of Chemistry*, 13(1), 916-931.
29. Noukelag, S.K.; Mohamed, H.E.A.; Razanamahandry, L.C.; Ntwampe S.K.O.; and Arendse, C.J. (2021). Bio-inspired synthesis of PbO nanoparticles (NPs) via an aqueous extract of Rosmarinus officinalis (rosemary) leaves. *Materialstoday Proceedings*, 36(2), 421-426.
30. Cortez-Valadez, M. ; Vargas-Ortiz, A.; Rojas-Blanco, L.; Arizpe-Chávez, H.; Flores-Acosta, M.; and Ramírez-Bon, R. (2013). Additional active Raman modes in α-PbO nanoplates. *Physica E: Low-dimensional Systems and Nanostructures*, 53, 146-149.
31. Staszewski, M.; Myczkowski, Z.; Bilewska, K.; Sosiński, R.; Lis, M.; Czepelak, M.; and Kołacz, D. (2012). High-energy milling as a method for obtaining tetragonal form of PbO. *Journal of Achievements in Materials and Manufacturing Engineering*, 52(1), 39-46.
32. El Sayed, A.M. and Morsi, W. M. (2013). Dielectric relaxation and optical properties of polyvinyl chloride/lead monoxide nanocomposites. *Polymer Composites*, 34(12), 2031-2039.
33. Canepa, P.; Ugliengo, P.; and Alfredsson, M. (2012). Elastic and Vibrational Properties of α- and β-PbO. *The Journal of Physical Chemistry C*, 116, 21514-21522.
34. Mythili, N. and Arulmozhi, K.T. (2014). Characterization Studies on the Chemically Synthesized α and β Phase PbO Nanoparticles. *International Journal of Scientific & Engineering Research*, 5(1), 412-416.
35. Shojaei, M.; Shokuhfar, A.; and Zolriasatein, A. (2021). Synthesis and characterization of CuAlS2 nanoparticles by mechanical milling. *Materials Today Communication*, 27, 102243.
36. Echevarria-Bonet, C.; Rojas, D.P.; Espeso, J.I.; Fernández, J.R.; Rodríguez, M. de la F.; Barquín, L.F.; Fernández, L.R.; Gorria, P.; Blanco, J.A.; Fdez-Gubieda, M.L.; Bauer, E.; and Damay, F. (2015). Magnetic phase diagram of superantiferromagnetic TbCu2 nanoparticles. *Journal of Physics: Condensed Matter*, 27, 496002.
37. Gusev, A.I. and Kurlov, A.S. (2008). Production of nanocrystalline powders by high-energy ball milling: model and experiment. *Nanotechnology*, 19, 265302.
38. Jefremovas,E.M.; Alonso, J.; de la Fuente Rodríguez, M.; Rodríguez Fernández, J.; Espeso, J.I.; Rojas, D.P.; García-Prieto, A.; Fernández-Gubieda, M.L.; and Fernández Barquín, L. (2020). Investigating the Size and Microstrain Influence in the Magnetic Order/Disorder State of GdCu2 Nanoparticles. *Nanomaterials*, 10, 1117.
39. Mathew, B.B. and Krishnamurthy, N.B. (2018). Evaluation of lead oxide nanoparticles synthesized by chemical and biological methods. *Journal of Nanomedicine Research*, 7(3), 195-198.

40. Akimov, D.V.; Andrienko, O.S.; Egorov, N.B.; Zherin, I.I.; and Usov, V.F. (2012). Synthesis and properties of lead nanoparticles. *Russian Chemical Bulletin*, 61, 225-229.
41. Arulmozhi, K.T.; and Mythili, N. (2013). Studies on the chemical synthesis and characterization of lead oxide nanoparticles with different organic capping agents. *AIP Advances*, 3(12), 122122.
42. Alagar, M.; Theivasanthi, T.; and Raja, A.K. (2012). Chemical Synthesis of Nano-sized Particles of Lead Oxide and their Characterization Studies. *Journal of Applied Sciences*, 12(4), 398-401.
43. Rashed, H.H.; Fadhil, F.A.; and Hadi, I.H. (2017). Preparation and Characterization of Lead Oxide Nanoparticles by Laser Ablation as Antibacterial Agent. *Baghdad Science Journal*, 14(4), 801-807.
44. Udvardi, B.; Kovacs, I.J.; Fancsik, T.; Konya, P.; Batori, M.; Stercel, F.; Falus, G.; and Szalai, Z. (2016). Effects of Particle Size on the Attenuated Total Reflection Spectrum of Minerals. *Applied Spectroscopy*, 71(6), 1157-1168.
45. Myers, T.L.; Brauer, C.S.; Su, Y.; Blake, T.A.; Johnson, T.J.; and Richardson, R.L. (2014). The influence of particle size on infrared reflectance spectra. *Algorithms and Technologies for Multispectral, Hyperspectral, and Ultraspectral Imagery XX SPIE*, 9088, 61-68.
46. Wankasi, D. and Dikio, E.D. (2014). Comparative Study of Polystyrene and Polymethylmethacrylate Wastes as Adsorbents for Sorption of Pb2+ from Aqueous Solution. *Asian Journal of Chemistry*, 26(4), 8295-8302.
47. Güngör, A.; Genç, R.; and Özdemir, T. (2017). Facile Synthesis of Semiconducting Nanosized 0D and 2D Lead Oxides Using a Modified Co-Precipitation Method. *Journal of the Turkish Chemical Society Section A: Chemistry*, 4(3): 1017-1030.
48. Dominguini, L.; da Rosa, R.G.; Martinello, K.; Pizzolo, J.P.; and Fiori, M.A. (2015). Thermal behavior of composites of PS-LDH (Mg-Al) modified with SDB and SDS. *Polímeros*, 25, 25-30.
49. Bagheri, K.; Razavi, S M.; Ahmadi, S J.; Kosari, M.; and Abolghasemi, H. (2017). Thermal resistance, tensile properties, and gamma radiation shielding performance of unsaturated polyester/nanoclay/PbO composites. *Radiation Physics and Chemistry*, 146, 5-10.
50. Shalu, S.; Dasgupta, K.; Roy, S.; Kar, P.; Bal, T.; and Ghosh, B.Da. (2020). Thermal, mechanical, and dielectric properties of low loss $PbZr_{0.3}Ti_{0.7}O_3$/polystyrene composites prepared by hot-press method. *Polymer Composites*, 42(3), 1420-1428.
51. Botan, R.; Nogueira, T.R.; Wypych, F.; and Lona, L.M.F. (2012). In situ synthesis, morphology, and thermal properties of polystyrene—MgAl layered double hydroxide nanocomposites. *Polymer Engineering and Science*, 52(8), 1754-1760.
52. Japic, D.; Marinsek, M.; and Orel, Z.C. (2016). Effect of ZnO on the Thermal Degradation Behavior of Poly(Methyl Methacrylate) Nanocomposites. *Acta Chimica Slovenica*, 63(3), 535-543.
53. Broido, A. (1969). A Simple, Sensitive Graphical Method of Treating Thermogravimetric Analysis Data. *Journal of Polymer Science: Part A-2*, 7, 1761-1773.

54. Chigwada, G.; Kandare, E.; Wang, D.; Majoni, S.; Mlambo, D.; Wilkie, C.A.; and Hossenlopp, J.M. (2008). Thermal Stability and Degradation Kinetics of Polystyrene/Organically-Modified Montmorillonite Nanocomposites. *Journal of Nanoscience and Nanotechnology*, 8(4), 1927-1936.
55. Tippaha, K.; Jittangkoon, N.; and Cherntongchai, P. (2016). Model-free Kinetic Analysis of Thermal Degradation of Polystyrene and High-Density Polyethylene Blends, *Chiang Mai Journal of Science*, 43(2), 296-305.
56. Pierella, L.B.; Renzini, S.; Cayuela, D.; and Anunziata, O.A. (2006). Catalytic Degradation of Polystyrene Over ZSM-11 Modified Materials. *Second Mercosur Congress on Chemical Engineering*, *4th Mercosur Congress on Process Systems Engineering*, Costa Verde, Brazil, 1-8.
57. Rieger, J. (1996). The glass transition temperature of polystyrene, Results of a round robin test. *Journal of Thermal Analysis*, 46, 965-972.
58. Barzegari, M.R.; Alemdar, A.; Zhang, Y.; and Rodrigue, D. (2013). Thermal Analysis of Highly Filled Composites of Polystyrene with Lignin. *Polymers & Polymer Composites*, 21(6), 357-366.
59. Worzakowska, M. (2015). Thermal and mechanical properties of polystyrene modified with esters derivatives of 3-phenylprop-2-en-1-ol. *Journal of Thermal Analysis and Calorimetry*, 121, 235-243.
60. Mahmoud, M.E.; El-Khatib, A.M.; Badawi, M.S.; Rashed, A.R.; El-Sharkawy, R.M.; and Thabet, A.A. (2017). Fabrication, characterization and gamma rays shielding properties of nano and micro lead oxide-dispersed-high density polyethylene composites. *Radiation Physics and Chemistry*, 145, 160-173.
61. Sohel, Md.A.; Mandal, A.; Mondal, A.; Pan, S.; and SenGupta, A. (2018). Calorimetric Analysis of Uncompatibilized Polypropylene/Polystyrene Blend Using DSC. *Macromolecular Symposia*, 379(1), 1700032.
62. Obeid, A.; Roumie, M.; Badawi, M.S.; and Awad, R. (2022). Evaluation of the Effect of Different Nano-Size of WO3 Addition on the Thermal Properties of HDPE Composite. *International Journal of Thermophysics*, 43, 37.